INTERNATIONAL JOURNAL FOR NUMERICAL METHODS IN FLUIDS
Int. J. Numer. Meth. Fluids 2000; **34**: 371–401

An algorithm for unsteady viscous flows at all speeds

Ivan Mary[a], Pierre Sagaut[a,*,1] and Michel Deville[b]

[a] *ONERA, av. de la Division Leclerc, Châtillon Cedex, France*
[b] *Laboratory of Fluid Mechanics, EPFL, Lausanne, Switzerland*

SUMMARY

An algorithm for the simulation of unsteady, viscous, stratified compressible flows, which remains valid at all speeds, is presented. The method is second-order accurate in both space and time and is independent of the Mach number. In order to remove the stiffness of the numerical problem due to the large disparity between the flow speed and the acoustic wave speed at low Mach number, an approximate Newton method, based on artificial compressibility, is proposed. Additionally, a modified advection upstream splitting method (AUSM+) scheme is used, which permits accurate computations of both compressible and incompressible flows. A detailed description of the method and an efficiency comparison with other approximate Newton methods described in the literature are given. Furthermore, it is shown that the accuracy of the algorithm is not dependent on the Mach number through the computations of various benchmark test cases. Copyright © 2000 John Wiley & Sons, Ltd.

KEY WORDS: all speed flow; AUSM+; quasi-Newton; unsteady problem

1. INTRODUCTION

Over the past years, unified numerical methods have been developed in the hope of solving compressible and incompressible flow problems using a single model. The need for unique numerical schemes that simulate both low- and high-speed flows has become increasingly apparent. For instance, when large temperature variations are present in low-speed flows, as in many combustion problems, incompressible models are insufficient as these temperature variations lead to significant compressibility effects, even at low Mach numbers. Additionally, the engineering community prefers to use a unique code to deal with the broad range of flow conditions. Greater unification is achieved if the scheme preserves the possibility of time-accurate unsteady computations; however, this prohibits the use of recent preconditioning methods [1–4]. Indeed, this approach fails in cases of unsteady applications in spite of its efficiency to compute steady, nearly incompressible flows with compressible models, since the

* Correspondence to: ONERA, 29 av. de la Division Leclerc, 92322 Châtillon Cedex, France. Fax: +33 1 46734166.
[1] E-mail: sagaut@onera.fr

Received 20 April 1999
Revised 22 November 1999

transient behavior of the Navier–Stokes equations is modified. The main difficulty in solving the compressible, unsteady equations at a low Mach number is due to the large disparity between the acoustic wave speed and the advection velocity. Therefore, an implicit temporal discretization must be used otherwise a severe stability restriction results on the time step. This is due to the fact that numerical stability considerations impose small time steps on the acoustic waves, while the physics is mainly driven by the main flow, where the time scale is large. Only three kinds of implicit methods that preserve the possibility of unsteady applications at all speeds are described in the literature. The first one, which is at most second-order accurate in time, is based on Strang's splitting [5] of the Navier–Stokes equations into two sub-systems. One sub-system contains the acoustic part, where an implicit method is used for the integration, and the other is integrated by an explicit scheme. Erlebacher *et al.* [6] successfully used this technique to compute isotropic homogeneous turbulence at low Mach numbers. However, the extension to non-homogeneous flow conditions is not straightforward and very few attempts have been reported [7]. The second approach, which is only first-order accurate in time, is based on an extension of projection methods to compressible flows [8–10]. Finally, the third method is built on dual-time stepping integration procedures [11–17].

The work presented here is based on the third method, which is in fact equivalent to an approximate Newton method, and can achieve second-order accuracy in time. Since a fully implicit temporal discretization is used, the time step can be determined only by physical criteria and accuracy considerations. However, contrary to References [11–17], a second-order accurate shock-capturing scheme is employed on a collocated grid in order to achieve a higher degree of polyvalency. Also, different Newton approximations are considered to gain better computational efficiency. Since the accuracy of standard shock-capturing schemes degrades at low Mach number [18], a modified AUSM + scheme, developed by Edwards and Liou [19] for all speed steady flows, is employed. Other shock-capturing schemes, such as modified Roe or Jameson schemes [20,21], could be used as well. However, we retain the modified AUSM + scheme because it seems to realize a good compromise between accuracy and complexity. Some simplifications are achieved in the Newton approximations by neglecting all off-diagonal terms, which do not contribute to the pressure/velocity coupling nor to the stabilization of high-Reynolds number flows. Despite the slower convergence of the Newton process, computational efficiency is improved. Indeed, as Bi-CGSTAB [22] is used to solve the linear system associated with the Newton process, the above approximations allow for a better conditioning and a faster matrix/vector product, while the storage requirements remain reasonable. Another crucial approximation is introduced in the Jacobian, for low-Mach number flows, by using an adaptation of artificial compressibility methods [23]. This leads to a better computational efficiency [24] when compared with the use of the preconditioning matrix developed for steady, nearly incompressible flows [11–13,15].

In Section 2, a set of equations valid at all Mach numbers and consistent with the full compressible conservative Navier–Stokes equations is given. The numerical method, as well as the spatial and temporal discretizations and the approximate Newton method are described in Section 3. Section 4 is devoted to an efficiency comparison between the present method and other approximate Newton methods [11,12]. Guidelines are indicated for the choice of optimal numerical parameters associated with artificial compressibility. Finally, the efficiency of the proposed scheme is compared with numerical benchmarks for a broad range of laminar flow

conditions in Section 5. The spatial and temporal accuracy of the scheme is evaluated in the nearly incompressible regime, by computing vortex shedding past a square cylinder. The ability to compute incompressible stratified flow with large temperature variations is assessed through the computation of Rayleigh–Bénard flow. The behavior of the algorithm is also studied in the subsonic and transsonic regimes through the computations of mixing layer and the interaction between shock and temperature spots. No fully supersonic flow has been computed because the spatial discretization reduces to the standard AUSM+ scheme, which has a proven efficiency in such a flow regime [25,26].

2. GOVERNING EQUATIONS

2.1. Dimensionless form

The two-dimensional unsteady Navier–Stokes equations are used for a viscous compressible Newtonian fluid. A dimensionless form of the equations is retained. The non-dimensional variables are defined from the physical variables as follows:

$$u_i = \frac{u_i^*}{u_0}, \quad T = \frac{T^*}{T_0}, \quad \rho = \frac{\rho^*}{\rho_0}, \quad p = \frac{p^*}{\rho_0 u_0^2}, \quad t = \frac{t^* u_0}{L_0}, \quad \mu = \frac{\mu^*}{\mu_0}, \quad k = \frac{k^*}{k_0}, \quad g = \frac{g^*}{g_0} \tag{1}$$

where the symbols u_0, T_0, ρ_0, L_0, μ_0, k_0, and g_0 denote a characteristic velocity, temperature, density, length, dynamic viscosity, thermal conductivity, and gravity respectively. Also, the subscript 0 and superscript * indicate the charateristic and dimensional quantities respectively.

Several dimensionless numbers are defined as

$$Re = \frac{\rho_0 u_0 L_0}{\mu_0}, \quad Pr = \frac{\mu_0 C_p}{k_0}, \quad M_0^2 = \frac{u_0^2}{\gamma R T_0}, \quad Ra = \frac{g_0 L_0^3 C_p \Delta T}{\mu_0 k_0 T_0}, \quad Fr = \frac{g_0 L_0}{u_0^2} = \frac{Ra T_0}{Re^2 Pr \Delta T} \tag{2}$$

where ΔT is a characteristic temperature variation of the flow and γ is the ratio of the specific heat capacities (1.4 for air). Re is the Reynolds number, Pr the Prandtl number, M_0 the reference Mach number, Ra the Rayleigh number, and Fr the Froude number. The conservative form of the Navier–Stokes equations written in Cartesian co-ordinates can be expressed as

$$\frac{\partial Q_c}{\partial t} + \frac{\partial (E_j - E_j^v)}{\partial x_j} = H \tag{3}$$

where the vectors Q_c, E_j, E_j^v, and H are defined as

$${}^t Q_c = (\rho, \rho u_1, \rho u_3, \rho e)$$

$${}^t E_j = (\rho u_j, \rho u_1 u_j + \delta_{1j} p, \rho u_3 u_j + \delta_{3j} p, (\rho e + p) u_j)$$

$$^tE_v = \left(0,\ \tau_{1j},\ \tau_{j3},\ u_1\tau_{1j} + u_3\tau_{j3} + \frac{\mu}{RePr(\gamma-1)M_0^2}\frac{\partial T}{\partial x_j}\right)$$

$$^tH = (0,\ 0,\ -Fr\rho,\ -Fr\rho u_3)$$

$$\rho e = \frac{p}{\gamma - 1} + \frac{1}{2}\rho u_k u_k$$

$$\tau_{ij} = \frac{\mu}{Re} S_{ij}$$

$$S_{ij} = \frac{\partial u_i}{\partial x_j} + \frac{\partial u_j}{\partial x_i} - \frac{2}{3}\delta_{ij}\frac{\partial u_k}{\partial x_k}$$

Summation over the repeated indexes is assumed with $j = 1$ or $j = 3$. The superscript 't' indicates the transposed vectors. The fluid is supposed to be an ideal gas satisfying the equation of state

$$p = \frac{\rho T}{\gamma M_0^2} \tag{4}$$

The dynamic viscosity μ is determined by Sutherland's equation

$$\mu = \frac{1+c}{1+T} T^{3/2} \tag{5}$$

where c depends on the fluid and the reference temperature.

2.2. All Mach number formulation

A significant source of error at low Mach numbers is due to the fact that the mean level of the pressure is of order $1/\gamma M_0^2$ (see Equation (4)). As a consequence, round-off errors can appear in the calculation of the pressure gradient in the momentum equations. To prevent this problem the pressure can be decomposed into static and dynamic parts [11,27]. Likewise, only the deviation of density from its static state is considered in the stratification term. The static state is determined by setting all unsteady terms and velocity to zero in Equation (3). This static state, denoted by the subscript 's', is defined as

$$\frac{\partial}{\partial x_j}\left(\mu\frac{\partial T_s}{\partial x_j}\right) = 0, \qquad \frac{\partial p_s}{\partial x_3} = -Fr\rho_s, \qquad p_s = \frac{\rho_s T_s}{\gamma M_0^2} \tag{6}$$

An analytical solution of these equations is proposed by Spiegel [28] in the case of constant viscosity. The dynamic part of the pressure maintains a value of the order of unity, and no significant round-off errors are produced as long as the dynamic pressure, instead of the total pressure, is retained as a variable.

From Equation (4), dynamic pressure p_{dyn} is defined as follows:

$$p(x, z, t) = p_{\mathrm{s}}(z) + p_{\mathrm{dyn}}(x, z, t) \tag{7}$$

and the equation of state becomes

$$\rho(x, z, t) = \frac{(p_{\mathrm{s}} + p_{\mathrm{dyn}})\gamma M_0^2}{T} \tag{8}$$

In order to achieve good property conservation in the transsonic flow conditions, the conservative form of the energy equation must be retained

$$\frac{\partial \rho E}{\partial t} + \frac{\partial (\rho E + p)u_j}{\partial x_j} - \frac{C_p}{RePr}\frac{\partial}{\partial x_j}\left(\mu \frac{\partial T}{\partial x_j}\right) - \frac{\partial \tau_{ij} u_i}{\partial x_j} + Fr\rho u_3 = 0 \tag{9}$$

However, the pressure/temperature form of the energy equation, which is equivalent to Equation (9) at the continuum level, is better suited for incompressible flow conditions

$$\rho C_p d_t(T) - d_t(p) - \frac{C_p}{RePr}\frac{\partial}{\partial x_j}\left(\mu \frac{\partial T}{\partial x_j}\right) - \tau_{ij}\frac{\partial u_i}{\partial x_j} + u_i\left(\frac{\partial \rho u_i}{\partial t} + \frac{\partial \rho u_i u_j}{\partial x_j} + \frac{\partial p_d}{\partial x_i} - \frac{\partial \tau_{ij}}{\partial x_j} + Fr\rho\delta_{i3}\right)$$
$$+ \frac{u_i u_i}{2}\left(\frac{\partial \rho}{\partial t} + \frac{\partial \rho u_j}{\partial x_j}\right) + C_p T\left(\frac{\partial \rho}{\partial t} + \frac{\partial \rho u_j}{\partial x_j}\right) = 0 \tag{10}$$

where d_t denotes the material time derivative and C_p the heat capacity at constant pressure.

The three last terms of Equation (10) are not implemented in incompressible methods as they are equal to zero at the continuum level. As a consequence, the use of both Equation (9) and a numerical method based on the Newton process can lead to inaccurate simulation in the low-Mach number regime. Indeed, for efficiency reasons, the Newton process does not fully converge at each time step. Thus, Equations (9) and (10) are no longer equivalent numerically as the three last terms of Equation (10) are proportional to $\epsilon_{\mathrm{Newton}}$, which is the convergence criterion of the Newton process. More particularly, the term

$$C_p T\left(\frac{\partial \rho}{\partial t} + \frac{\partial \rho u_j}{\partial x_j}\right)$$

in Equation (10) can slightly differ from zero, since it is of order $C_p \epsilon_{\mathrm{Newton}}$ with $C_p = [(\gamma - 1)M_0^2]^{-1}$. As a consequence, this term is subtracted from the conservative form of the energy equation in order to produce an accurate solution in both transsonic and nearly incompressible flow conditions. The new set of equations, which must be integrated to solve the compressible Navier–Stokes equations at all Mach numbers, is written as

$$f = 0 \tag{11}$$

where

$$f = \begin{pmatrix} f_1 \\ f_2 \\ f_3 \\ f_4 \end{pmatrix} = \begin{pmatrix} \dfrac{\partial \rho}{\partial t} + \dfrac{\partial \rho u_j}{\partial x_j} \\ \dfrac{\partial \rho u_1}{\partial t} + \dfrac{\partial \rho u_1 u_j}{\partial x_j} + \dfrac{\partial p_{\mathrm{dyn}}}{\partial x_1} - \dfrac{\partial \tau_{1j}}{\partial x_j} \\ \dfrac{\partial \rho u_3}{\partial t} + \dfrac{\partial \rho u_3 u_j}{\partial x_j} + \dfrac{\partial p_{\mathrm{dyn}}}{\partial x_3} - \dfrac{\partial \tau_{j3}}{\partial x_j} + Fr(\rho - \rho_s) \\ \dfrac{\partial \rho e}{\partial t} + \dfrac{\partial (\rho e + p) u_j}{\partial x_j} - \dfrac{C_p}{RePr} \dfrac{\partial}{\partial x_j} \left(\mu \dfrac{\partial T}{\partial x_j} \right) - \dfrac{\partial \tau_{ij} u_i}{\partial x_j} + Fr \rho u_3 - C_p T f_1 \end{pmatrix} \tag{12}$$

3. NUMERICAL METHOD

3.1. Spatial and temporal discretization

The spatial discretization can be made on both a staggered or collocated grid. The staggered grid is well adapted to the computation of very low Mach numbers as the pressure/velocity coupling is ensured by the marker-and-cell (MAC) discretization. However, despite the recent progress from the work of Bijl and Wesseling [10], the implementation of accurate shock-capturing schemes is not straightforward. Consequently, the spatial discretization is obtained by a node-centered finite volume technique on a collocated grid. This, in turn, is well adapted to the use of shock-capturing schemes. The semi-discrete form of Equation (11) can be written as follows:

$$\frac{\partial Q_{c\ i,k}}{\partial t} + R_{i,k} = H^{\mathrm{mod}}_{i,k} \tag{13}$$

where 'i, k' indicate the collocation point, $H^{\mathrm{mod}} = {}^{t}H + {}^{t}(0, 0, Fr\rho_s, C_p T f_1)$, and R represents the spatial derivative of the Euler and viscous fluxes

$$R_{i,k} = \sum_{j=1 \text{ or } 3} \frac{(E_j - E_j^v)_{i+1/2\delta_{1j},\, k+1/2\delta_{3j}} - (E_j - E_j^v)_{i-1/2\delta_{1j},\, k-1/2\delta_{3j}}}{\Delta x_j(i,k)} \tag{14}$$

where $i + 1/2\delta_{1j}, k + 1/2\delta_{3j}$ refers to a cell interface. However, although this discretization method is an accepted technique for transsonic flows, current shock-capturing schemes must often be modified to preserve their accuracy on the whole range of Mach numbers. Indeed, the numerical dissipation of shock-capturing schemes is often based on $|u| + c$ (Roe, Jameson, . . .), where c is the speed of sound. Thus, the accuracy of the solution is deteriorated when the speed of sound becomes large in the incompressible regime [18,20,29]. The shock-capturing scheme utilized here is the AUSM+ scheme [25], which has been modified by

Edwards and Liou [19] to preserve its accuracy and the pressure/velocity coupling in the nearly incompressible regime. This flux-vector splitting scheme is chosen because it seems to reach a better compromise between accuracy and efficiency than other shock-capturing schemes recently developed [20,21].

In the x_1-direction, the AUSM+ scheme leads to the following splitting of the Euler flux at the cell interface $i+1/2, k$ (the index k is omitted for the case of notation):

$$E_{1\ i+1/2} = F_{i+1/2}(M_L, M_R) + p_{i+1/2}(M_L, M_R)\ {}^t(0, 1, 0, 0) \tag{15}$$

with $\Phi_{L/R}$ indicating the left or right interpolation of the variable Φ at the cell interface, and M representing the local value of the Mach number. In Equation (15), the quantities on the right-hand side are computed as

$$F_{i+1/2}(M_L, M_R) = [\mathscr{M}_4^+(M_L) + \mathscr{M}_4^-(M_R)]c_{i+1/2} \begin{pmatrix} \rho \\ \rho u_1 \\ \rho u_3 \\ \rho e + p \end{pmatrix}_{L/R} \tag{16}$$

$$p_{i+1/2}(M_L, M_R) = \mathscr{M}_5^+(M_L)p_L + \mathscr{M}_5^-(M_R)p_R \tag{17}$$

with $c_{i+1/2}$ the speed of sound at the interface [23] and

$$\mathscr{M}_1^{\pm}(M) = 0.5(M \pm |M|)$$

$$\mathscr{M}_4^{\pm}(M) = \begin{cases} \pm 0.25(M \pm 1)^2 \pm 0.125(M^2-1)^2, & \text{if } |M| \le 1 \\ \mathscr{M}_1^{\pm}(M), & \text{otherwise} \end{cases}$$

$$\mathscr{M}_5^{\pm}(M) = \begin{cases} 0.25(M \pm 1)^2(2 \mp M) \pm \frac{3}{16}M(M^2-1)^2, & \text{if } |M| \le 1 \\ 0.5(1 \pm |M|/M), & \text{otherwise} \end{cases}$$

In the low-speed zone, the numerical dissipation contained in Equation (16) goes to zero. This tends to decrease the robustness of the method. However, in Equation (17), the dissipation goes to infinity when the reference Mach number M_0 is small. In order to solve these problems, some modifications were introduced by Edwards and Liou [19]. These modifications led to a new definition of the interface Euler flux

$$E_{1\ i+1/2}^{\text{mod}} = F_{i+1/2}^{\text{mod}}(\bar{M}_L, \bar{M}_R) + p_{i+1/2}^{\text{mod}}{}^t(0, 1, 0, 0) \tag{18}$$

where

$$F^{\mathrm{mod}}_{i+1/2}(\bar{M}_{\mathrm{L}}, \bar{M}_{\mathrm{R}}) = F_{i+1/2}(\bar{M}_{\mathrm{L}}, \bar{M}_{\mathrm{R}})h_{i+1/2} + (\mathscr{M}_4^+(\bar{M}_{\mathrm{L}}) - \mathscr{M}_1^+(\bar{M}_{\mathrm{L}}) - \mathscr{M}_4^-(\bar{M}_{\mathrm{R}}) + \mathscr{M}_1^-(\bar{M}_{\mathrm{R}})) \times h_{i+1/2}c_{i+1/2}\left(\frac{1}{\alpha_{i+1/2}} - 1\right)(p_{\mathrm{L}} - p_{\mathrm{R}})\frac{K_1\gamma M_0^2}{T_i + T_{i+1}}{}^t(1, u_1, u_3, e + p/\rho)_{\mathrm{L/R}}$$

$$p^{\mathrm{mod}}_{i+1/2}(\bar{M}_{\mathrm{L}}, \bar{M}_{\mathrm{R}}) = p_{i+1/2}(\bar{M}_{\mathrm{L}}, \bar{M}_{\mathrm{R}}) \tag{19}$$

and

$$\alpha_i = \mathrm{Min}[1, c_i^{-2}\,\mathrm{Max}[|u|^2, K_2]], \qquad h_{i+1/2} = ((1 - \alpha_{i+1/2})M^2_{i+1/2} + 4\alpha_{i+1/2})^{1/2}(1 + \alpha_{i+1/2})^{-1}$$

The values of $\alpha_{i+1/2}$ and $M_{i+1/2}$ are obtained by a simple arithmetic average and

$$\bar{M}_{\mathrm{L/R}} = (c_{i+1/2}h_{i+1/2})^{-1}((1 + \alpha_{i+1/2})u_{\mathrm{L/R}} + (1 - \alpha_{i+1/2})u_{\mathrm{R/L}})$$

The constants K_1 and K_2 are numerical parameters. In Equation (19), the second term allows for pressure/velocity coupling at low values of the reference Mach number M_0. The modification of Equation (17) involves accurate simulation of nearly incompressible flows, while maintaining robustness of the scheme at high Reynolds number. Note here that Edwards and Liou [19] set (K_1, K_2) equal to $(1, 0.25)$ respectively. In this work, slightly different values are retained: $(K_1, K_2) = (0.1, 0.04)$. Numerical experiments have shown that, on the one hand, the pressure/velocity coupling and the stabilization of high-Reynolds number flows are still achieved in spite of the reduction of the numerical dissipation. On the other hand, the implicit temporal integration is made easier by a slight modification of the system conditioning. The definition of α proposed by Edwards and Liou [19], which takes into account the eigenvalues of the preconditioned system [1–3], is used in this work. As we will demonstrate, favorable results are reached despite the fact that no time derivative preconditioning technique is used. A possible explanation is that the main feature of α is a proper scaling of the numerical dissipation, independently of the temporal derivative terms [30]. For supersonic flow conditions, the modified scheme retrieves the standard form of the AUSM+ method, which has already proven efficiency in this case [25,26]. As for the evaluation $\Phi_{\mathrm{L/R}}$, a third-order accurate interpolation is used, and a Minmod limiter [31] is employed for transsonic flows to deal with the presence of shocks. For the diffusive fluxes, the spatial discretization is achieved by central second-order derivative approximations.

For the temporal discretization, an implicit scheme must be used to develop an algorithm where the time step is governed by the physics rather than by numerical stability considerations. Otherwise, in the nearly incompressible regime, the value of the time step is governed by the acoustic wave speed, while the physics are mainly driven by the underlying flow, where the time scale is large. Then, the temporal derivative of Q_c in Equation (13) is discretized by a three-level backward differentiation formula

$$\frac{\partial Q_c}{\partial t} \approx \frac{3Q_c^{n+1} - 4Q_c^n + Q_c^{n-1}}{2\Delta t} = D_t(Q_c) \tag{20}$$

whereas Euler, viscous fluxes, and H^{mod} are estimated at $n+1$. With Δt being the time step, the superscript n denotes the physical time ($t_n = t_{\text{initial}} + n\Delta t$, $Q_c^n = Q_c(t_n)$). This differentiation is second-order accurate and possesses good stability properties [32]. With Equation (20) and the modified AUSM+ scheme, a discretized form of Equation (13) is obtained

$$D_t(Q_c^{n+1}) + R^{n+1} - H^{\text{mod } n+1} = 0 \tag{21}$$

For convenience, Equation (21) is written as

$$f_d(Q_c^{n+1}, Q_c^n, Q_c^{n-1}) = 0 \tag{22}$$

3.2. Approximate Newton method

An exact Newton method can be employed to solve Equation (22). This requires a choice of both a set of variables Q, used to linearize Equation (22) and an iterative procedure

$$\left[\frac{\partial f_d}{\partial Q}\right]_{|Q^l} \Delta Q = -f_d(Q_c^l, Q_c^n, Q_c^{n-1}) \tag{23}$$

where $\Delta Q = Q^{n+1,l+1} - Q^{n+1,l}$ is the lth iterate solution of the Newton process. For convenience, $Q^{n+1,l}$ is noted as Q^l and Equation (23) can be rewritten by using Equation (21)

$$\left(\frac{3}{2\Delta t}\left[\frac{\partial Q_c}{\partial Q}\right] + \left[\frac{\partial R}{\partial Q}\right] - \left[\frac{\partial H^{\text{mod}}}{\partial Q}\right]\right)_{|Q^l} \Delta Q = -f_d(Q_c^l, Q_c^n, Q_c^{n-1}) \tag{24}$$

To preserve the accuracy of Equation (20), the iterative procedure is stopped when the following constraint is satisfied [31]:

$$f_d(Q_c^l, Q_c^n, Q_c^{n-1}) \leq C\Delta t^2 = \epsilon_{\text{Newton}}, \quad \text{where } C \text{ is a constant vector with } \|C\|_2 = 1 \tag{25}$$

If Equation (23) is solved with sufficiently good precision, only one iteration of the Newton process is required to fill Equation (25). Unfortunately, an analytical formulation of the Jacobian matrix resulting from an exact linearization is at best very time consuming, and sometimes impossible to evaluate. Additionally, the efficiency of the linear system associated with Equation (23) and solved by an iterative procedure depends on the condition number of the system. This number, based on Euclidian matrix norms, is defined as [34]

$$\mathrm{Cond}_2\left(\left[\frac{\partial f_d}{\partial Q}\right]\right)=\frac{\lambda_{\max}\left(\left[\frac{\partial f_d}{\partial Q}\right]^t\left[\frac{\partial f_d}{\partial Q}\right]\right)}{\lambda_{\min}\left(\left[\frac{\partial f_d}{\partial Q}\right]^t\left[\frac{\partial f_d}{\partial Q}\right]\right)} \tag{26}$$

where $\lambda_{\max}$ and $\lambda_{\min}$ are the maximum and minimum eigenvalues respectively. The closer to unity the condition number is, the less expensive (in terms of number of iterations) the solving procedure of the linear system is. Unfortunately, since all variables are strongly coupled, the condition number associated with an exact Newton method is often large, even at a Courant–Friedrich–Lewy (CFL) number close to 1. The appropriate choice of Q is a first step towards optimizing the matrix complexity and its condition number. For transsonic unsteady flows, $Q = Q_c$ is a natural choice (see Reference [26] for instance), leading to a small condition number when the CFL number is close to unity. However, this choice implies round-off error problems in the nearly incompressible regime. Several authors [11–13] chose to employ the primitive variables $(p_{\mathrm{dyn}}, u_1, u_3, T)$ to alleviate round-off error problems. However, the structure of $[\partial Q_c/\partial Q]$ in Equation (24) is much more complex than the identity matrix, and the use of a small time step has a smaller definite influence on the condition number. Thus, a compromise is utilized in this work, with ${}^tQ = (p_{\mathrm{dyn}}, \rho u_1, \rho u_3, T)$. Indeed, the choice of p_{dyn} and T solves round-off error problems, and the simplicity of temporal derivative linearization, as well as the conditioning, is improved through the momentum equations. Also, the linearization of the temporal derivative in Equation (21) is obtained through the matrix M_t

$$M_t=\frac{3}{2\Delta t}\begin{bmatrix} \gamma M_0^2/T^l & 0 & 0 & -(\rho/T)^l \\ 0 & 1 & 0 & 0 \\ 0 & 0 & 1 & 0 \\ (1-\gamma)M_0^2 & 0 & 0 & \frac{4}{3}\rho^n-\frac{1}{3}\rho^{n-1} \end{bmatrix} \tag{27}$$

In fact, approximations are introduced in M_t by setting the contribution of the kinetic energy variations in the energy equation to zero (fourth line of M_t). Despite this choice of Q, the Jacobian matrix remains very complex and its condition number is still large. Therefore, a faster temporal integration is achieved (i.e. requiring less computing time), by using an approximate Newton method. This is based on the replacement of $[\partial f_d/\partial Q]$ in Equation (23) by a matrix L, which possesses a smaller condition number. However, a trade-off must be reached between the improvement of the condition number and the errors introduced in the Newton process by the approximation of $[\partial f_d/\partial Q]$ by L. On the one hand, the complexity of the matrix coefficients and its conditioning have decreased, rendering each solution of Equation (25) faster. On the other hand, the number of Newton iterations required to satisfy Equation (25) increases. Despite the increased number of iterations, the CPU cost per time step can be significantly reduced by a faster solution of the linear system and appropriate approximations.

Three levels of approximations are used in this work. The first one concerns the Euler fluxes equation (18), the exact linearization of which can be rewritten as

$$\left[\frac{\partial E_{1\,i+1/2}^{\mathrm{mod}}}{\partial Q}\right]_{|Q^l}\Delta Q=\sum_{p=-1}^{2}\left[\frac{\partial E_1^{\mathrm{mod}}(Q_{i-1},\ldots,Q_{i+2})}{\partial Q_{i+p}}\right]_{|Q^l}\Delta Q_{i+p} \tag{28}$$

To reduce the number of non-zero entries in the linear system, a first-order interpolation is used to estimate the right and left state in the linearization of the Euler fluxes in Equation (28). This leads to

$$\left[\frac{\partial E_{1\,i+1/2}^{\mathrm{mod}}}{\partial Q}\right]_{|Q^l}\Delta Q\approx\sum_{p=0}^{1}\left[\frac{\partial E_1^{\mathrm{mod}*}(Q_{i-1},\ldots,Q_{i+2})}{\partial Q_{i+p}}\right]_{|Q^l}\Delta Q_{i+p} \tag{29}$$

where $E_1^{\mathrm{mod}*}$ is evaluated with Equation (18) and a first-order interpolation at the interface of $p_{\mathrm{L/R}}$ and $Q_{c\,\mathrm{L/R}}$ in Equations (16) and (17). This approach is commonly employed [26,35,36] because it does not significantly affect the stability of the iterative process, and thus a better conditioning can be achieved. However, the number of non-zero entries due to the Jacobian matrices of the right-hand side in Equation (29), and the linearization of the viscous terms, remains large. Then, a second level of approximation is developed, as was done in Equation (27), by neglecting certain contributions. For the Euler fluxes, the numerical dissipation of the AUSM+ scheme can be replaced by the spectral radius of the Roe's matrix as was done in Reference [26]. However, the validity of this approach over the whole range of Mach numbers is not obvious. Therefore, approximations in the Jacobian matrix of the right-hand side in Equation (29) are constructed by neglecting all off-diagonal terms, which do not contribute to the pressure/velocity coupling or to the stabilization of high-Reynolds number flows. Thus, the right-hand side of Equation (29) is approximated by

$$\sum_{p=0}^{1}\left[\frac{\partial E_1^{\mathrm{mod}*}(Q_{i-1},\ldots,Q_{i+2})}{\partial Q_{i+p}}\right]\Delta Q_{i+p}\approx E_1^{+}\Delta Q_i+E_1^{-}\Delta Q_{i+1} \tag{30}$$

where

$$E_1^{+}=\begin{bmatrix} w_1^{+}C_1\gamma M_0^2+Dp_1 & f(\rho)/\rho_i & 0 & -w_1^{+}C_1\\ G_1p_{\mathrm{L}} & w_1^{+}C_1+Du_1/\rho_i & 0 & 0\\ 0 & 0 & w_1^{+}C_1 & 0\\ 0 & f(\rho T)/\rho_i & 0 & w_1^{+}C_1\rho_i \end{bmatrix}$$

$$E_1^{-}=\begin{bmatrix} w_1^{-}C_1\gamma M_0^2-Dp_1 & f(\rho)/\rho_{i+1} & 0 & -w_1^{-}C_1\\ G_1p_{\mathrm{R}} & w_1^{-}C_1-Du_1/\rho_{i+1} & 0 & 0\\ 0 & 0 & w_1^{-}C_1 & 0\\ 0 & f(\rho T)/\rho_{i+1} & 0 & w_1^{-}C_1\rho_{i+1} \end{bmatrix} \tag{31}$$

with

$$C_1=(\mathscr{M}_4^{+}(\bar{M}_{\mathrm{L}})+\mathscr{M}_4^{-}(\bar{M}_{\mathrm{R}}))c_{i+1/2}h_{i+1/2}$$

$$w_1^{\pm} = 0.5(1 \pm \mathrm{sign}(C_1)), \qquad f(\phi) = 0.5(w_1^{+}\phi_i + w_1^{-}\phi_{i+1})$$

$$Dp_1 = (\mathscr{M}_4^{+}(\bar{M}_L) - \mathscr{M}_1^{+}(\bar{M}_L) - \mathscr{M}_4^{-}(\bar{M}_R) + \mathscr{M}_1^{-}(\bar{M}_R))\left(\frac{1}{\alpha_{i+1/2}} - 1\right)\frac{h_{i+1/2}c_{i+1/2}R_1\gamma M_0^2}{T_i + T_{i+1}}$$

$$G_1 p_L = 0.5 + \frac{u_i + u_{i+1}}{2h_{i+1/2}c_{i+1/2}}\left(a^{+}\left(\frac{15}{16} + \frac{3}{16}\bar{M}_L^4 - \frac{10}{16}\bar{M}_L^2\right)\right) + \frac{b^{+}}{2}|\bar{M}_L|/\bar{M}_L$$

$$G_1 p_R = 0.5 - \frac{u_i + u_{i+1}}{2h_{i+1/2}c_{i+1/2}}\left(a^{-}\left(\frac{15}{16} + \frac{3}{16}\bar{M}_R^4 - \frac{10}{16}\bar{M}_R^2\right)\right) - \frac{b^{-}}{2}|\bar{M}_R|/\bar{M}_R$$

$$a^{+} = \mathrm{int}(1 - |\bar{M}_L|), \quad a^{-} = \mathrm{int}(1 - |\bar{M}_R|), \quad b^{+} = \mathrm{int}(|\bar{M}_L|), \quad b^{-} = \mathrm{int}(|\bar{M}_R|)$$

$$Du_1 = \frac{\alpha_{i+1/2}}{2h_{i+1/2}c_{i+1/2}}\left(p_L a^{+}\left(\frac{15}{16} + \frac{3}{16}\bar{M}_L^4 - \frac{10}{16}\bar{M}_L^2\right) + p_R a^{-}\left(\frac{15}{16} + \frac{3}{16}\bar{M}_R^4 - \frac{10}{16}\bar{M}_R^2\right)\right)$$

Numerical experiments have shown that Dp_1, which arises from the linearization of Equation (19), is crucial for the stability of the Newton process for low values of M_0. This is a direct consequence of the decoupling between pressure and velocity if Dp_1 is set to zero in Equation (31). Similarly, Du_1, proceeding from Equation (19), stabilizes the Newton process when low-speed zones are present in a flow at large Reynolds numbers. As for the linearization of H^{mod} in Equation (13), some approximations are introduced as well. The stratification terms are not taken into account by the matrix, and their implicit treatment is realized by Newton iterations only. The linearization of $T\partial_j(\rho u_j)$ is achieved by

$$\left[\frac{\partial(T\partial_j(\rho u_j))}{\partial Q}\right]_{|Q^l}\Delta Q \approx \partial_j(\rho u_j)^l \Delta T_i + T_i^l\left[\frac{\partial(\partial_j(\rho u_j))}{\partial Q}\right]_{|Q^l}\Delta Q \tag{32}$$

where the Jacobian matrix of the momentum field divergence in the second term of the right-hand side is approximated through the use of the first component of Equation (30). Also, $\partial_j(\rho u_j)^l$ is computed using the first component of Equation (19), with a third-order accurate interpolation. Regarding the viscous fluxes, an approximation of the Jacobian matrix $[\partial E_v/\partial Q]$ is achieved by the M_{viscous} matrix, described in Reference [17]. This matrix maintains the contributions of the cross-derivative terms. The linearization of the Euler fluxes in the x_3-direction is achieved in a similar way and the generalization of Equations (29)–(32) to all the collocation points leads to the M_{Euler} matrix. Then, the approximation of Equation (23) can be written as

$$M\Delta Q = (M_t + M_{\mathrm{Euler}} + M_{\mathrm{viscous}})\Delta Q = -f_d(Q_c^l, Q_c^n, Q_c^{n-1}) \tag{33}$$

The structure of M_t defined in Equation (27) is very important for the computational efficiency of unsteady flows. Indeed, in such cases, the time step employed is quite small, which leads to good conditioning (i.e., small condition number) of the linear system associated with Equation

(33). However, this beneficial matrix property is lost for nearly incompressible flow problems if the time step is based on the velocity rather than the wave speed. Indeed the first diagonal element of M_t vanishes for small values of M_0. To alleviate this problem, some researchers [11–14] introduced a third level of approximation in the computation of the Jacobian matrix, by adding a preconditioning matrix Γ, developed for the computation of steady nearly incompressible flows [1–4], to Equation (33). This approach is often called 'dual-time stepping integration', as these preconditioning matrices introduced a dual-time. It is, however, equivalent to an approximate Newton procedure. Still, these matrices contain approximations in each line of Equation (33), while only the first one needs to be modified to reduce the condition number at low Mach numbers. Thus, a better compromise between the reduction of the condition number and the increase of Newton approximations owing to Γ, can be obtained [24]. This can be done for unsteady, low-Mach number flow; for instance, by using an adaptation of the artificial compressibility method developed by Chorin [23]. Finally, the linear system solved at each iteration of the Newton process is

$$L\Delta Q \stackrel{\text{def}}{=} \left(\frac{3\beta}{2\Delta t}\,\Gamma + M\right)\Delta Q = -f_d(Q_c^l, Q_c^n, Q_c^{n-1}) \tag{34}$$

with

$$\Gamma = \begin{bmatrix} 1 & 0 & 0 & 0 \\ 0 & 0 & 0 & 0 \\ 0 & 0 & 0 & 0 \\ 0 & 0 & 0 & 0 \end{bmatrix} \tag{35}$$

The optimal value of the numerical parameter β is completely case-dependent, and must be adjusted to achieve the best compromise between the reduction of the matrix condition number in Equation (34) and the minimization of the approximations introduced in $[\partial f_d/\partial Q]$ by the matrix L. To solve the linear system associated with Equation (34), the Bi-CGSTAB iterative method [22], based on two matrix/vector products, is employed. Therefore, Dp_j, C_j, $G_j p_{\mathrm{L}}$, $G_j p_{\mathrm{R}}$, Du_j and $\hat{\partial}_j(\rho u_j)$, which are still complex, are stored during the computation of the right-hand side of Equation (23) to accelerate the matrix/vector product. As M_{viscous} does not require additional storage, a negligible additional cost in terms of memory is introduced, since the requirements are less than three main diagonals of L. Moreover, a Jacobi preconditioning is used to improve the efficiency of the Bi-CGSTAB. This leads to the following linear system:

$$D_L^{-1} L\Delta Q = -D_L^{-1} f_d(Q_c^l, Q_c^n, Q_c^{n-1}) \tag{36}$$

where D_L is the main diagonal of L.

3.3. Boundary conditions

Since all variables are located at the boundaries, the treatment of the boundary conditions is straightforward. For an isothermal wall, the velocity boundary condition is a no-slip condition and the temperature is fixed to a prescribed value. An adiabatic wall corresponds to $\partial T/\partial n = 0$ with $\partial/\partial n$ denoting the derivative normal to the boundary. At the outflow boundary, homogeneous Neumann conditions are used: $\partial \rho u_i/\partial n = \partial T/\partial n = 0$. A non-centered, second-order, three-point scheme is used to discretize normal derivatives at the boundary. The pressure at the boundary is determined by a non-centered, second-order derivative approximation applied to the continuity equation.

4. ASSESSMENT OF THE TEMPORAL INTEGRATION METHOD

4.1. Comparisons with other approximate Newton methods

Over the past years several approximate Newton methods [11,12] have been proposed for the computation of unsteady flows at low Mach numbers. In order to evaluate the efficiency of the present method compared with existing ones, a simple test case has been considered. This test case deals with the advection of a Taylor vortex, which permits assessment of the efficiency of the preconditioning matrices developed by Merkle et *al.* [1,11] or Pletcher [12].

The computational domain is a square of length 1. At time $t = 0$, the vortex is located in the middle of the domain ($x_1 = x_3 = 0.5$), and the advection velocity directed in the x_3-direction is equal to unity. The initial conditions are given by the relations

$$\begin{array}{l|l} u_1(x_1, x_3, t=0) = C_1 \exp(-C_2 r^2) & p_{\mathrm{dyn}}(x_1, x_3, t=0) = 0 \\ u_3(x_1, x_3, t=0) = 1 - C_1 \exp(-C_2 r^2) & T_{\mathrm{initial}}(x_1, x_3, t=0) = 1 \end{array} \tag{37}$$

with

$$C_1 = 0.3, \quad C_2 = 88.9, \quad r = \sqrt{(x_1 - 1/2)^2 + (x_3 - 1/2)^2}$$

This problem has been selected because the boundary conditions are periodic in both directions, making the study easier. The reference Mach number M_0 is set to 10^{-3} so that the efficiency of the preconditioning matrix (see Equation (35)) in the incompressible regime can be evaluated. The Reynolds number based on the length of the domain and the advection velocity is set to 10000. A uniform mesh is used with $\Delta x_1 = \Delta x_3 = 0.01$.

In order to compare the present preconditioning matrix with those of Merkle or Pletcher, denoted Γ^{Merkle} and $\Gamma^{\mathrm{Pletcher}}$ respectively, the numerical parameter β in Equation (35) must be related to the dual-time step $\Delta\tau$ introduced in References [11–13] through the following relation:

$$\Delta\tau = 2\Delta t/(3\beta) \tag{38}$$

Moreover, when Γ^{Merkle} or Γ^{Pletcher} is used for the time stepping, the term

$$C_p T\left(\frac{\partial \rho}{\partial t}+\frac{\partial \rho u_j}{\partial x_j}\right)$$

is not subtracted from the energy equation. The approximations used here in the Newton process are thus identical to those proposed in References [11–13].

The efficiency of the present method compared with those proposed by Shuen et *al.* [11] or Pletcher is illustrated in Figure 1, where the CPU time, normalized by the CPU time spent to reach $t=1$ with a three-stage explicit Runge–Kutta scheme [47], is plotted for two CFL numbers: 100 and 1000. Figure 1 shows that the present method is at least 5–6 times faster than algorithms described in the literature for both CFL numbers. Moreover, an optimal value of β exists, which strongly depends on the CFL number, although this value is nearly independent of the choice of the preconditioning matrix. Indeed, for a fixed value of β, the number of iterations required to solve the linear problem is much smaller with the present approach, and the number of Newton iterations is almost independent of the chosen preconditioning matrix (see Figure 2). This last property can be explained by the value of the coefficient acting on the pressure in the continuity equation. For a fixed value of β, this coefficient is nearly independent of the preconditioning matrix. This arises from the fact that the ratios between the Merkle or Pletcher coefficients and the coefficient of the present method are equal to $1/(u_l u_l)$ or $1/T$ respectively (with $u_l u_l$ and T very close to 1 for this test case).

The second advantage of the proposed method for unsteady flows is the improved accuracy of the temperature field prediction. For flow in an incompressible regime without heat addition, the temperature variations are proportional to M_0^2. A reference solution is obtained by setting ϵ_{Newton} to 10^{-8}. In this case, the results, presented in Figure 3 by the squared

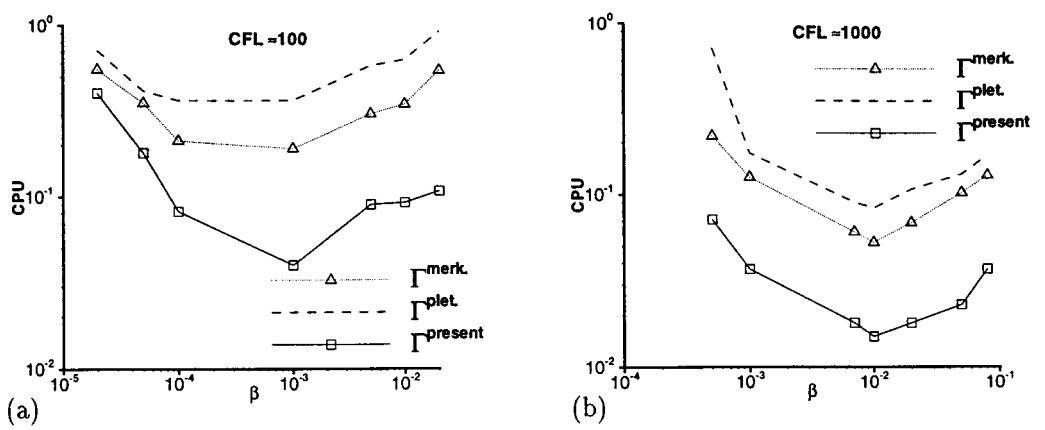

Figure 1. Taylor vortex advection: influence of the choice of the approximate Newton method on the efficiency of the temporal integration (normalized CPU time versus β).

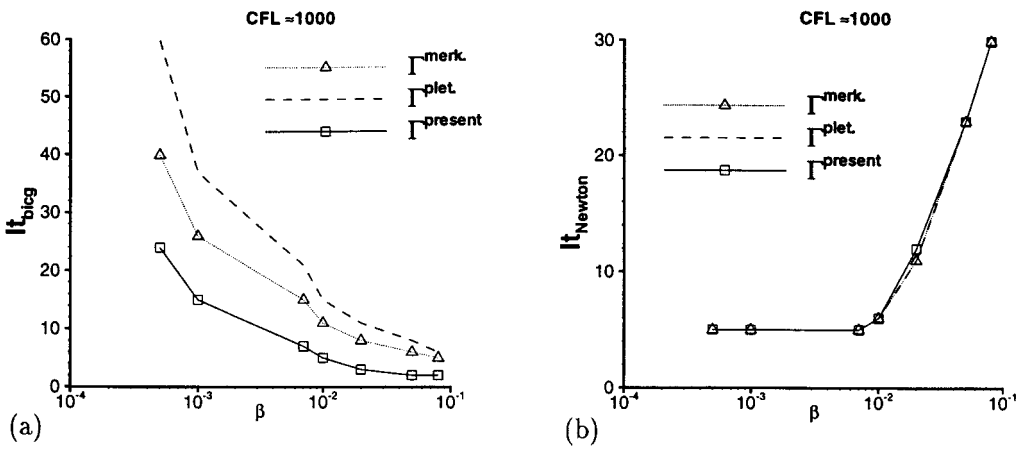

Figure 2. Taylor vortex advection: influence of the approximate Newton method choice and β on the average convergence of linear and non-linear processes for one time step integration at CFL = 1000 and $\epsilon_{\text{Newton}} = 10^{-4}$: (a) convergence of Bi-CGSTAB algorithm, (b) convergence of Newton process.

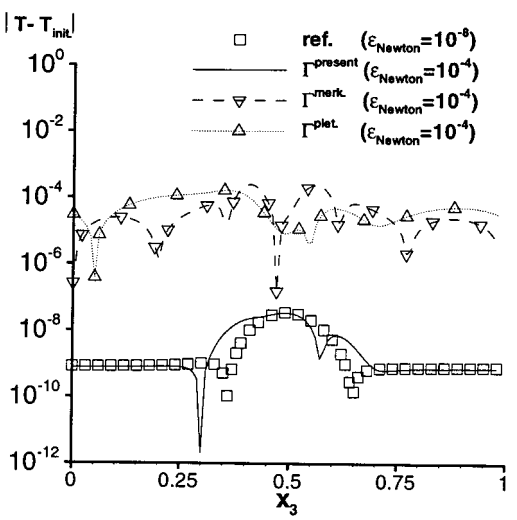

Figure 3. Taylor vortex advection: influence of the approximate Newton method choice and the Newton convergence criterion on the accuracy of the temperature fluctuations ($|T - T_{\text{initial}}|$ versus x_3 at $x_1 = 0.5$ and $t = 1$).

symbols, are independent of the preconditioning matrix. However, for $\epsilon_{\text{Newton}} = 10^{-4}$, the prediction of the temperature fluctuations becomes dependent on the choice of the temporal integration method. Figure 3 shows that these temperature variations could be much greater than M_0^2 if the convergence criterion of the Newton process is too large when Γ^{Pletcher} or Γ^{Merkle} is used. Note that, due to the all-Mach number formulation, the present method allows for a much more accurate solution, even if a large value of ϵ_{Newton} is used. Since the use of higher values of the convergence criterion in the Newton process leads to a significant reduction in computational time, it appears that the present method is better suited to the computation of stratified incompressible flow (often governed by very small temperature variations) when compared with approximate Newton methods described in the literature [11–13].

4.2. Influence of the flow regime and mesh refinement

As shown in the previous section, the efficiency of the proposed algorithm strongly depends on the choice of β. Moreover, the optimal value of β, denoted β_{opt}, is a function of the CFL number and the reference Mach number. In contrast with previous work [14,16], Γ is only introduced to treat the stiffness of nearly incompressible flows. Numerical instabilities of Bi-CGSTAB owing to mesh refinement and viscous effects are treated by the Jacobi preconditioning, which does not introduce another Newton approximation in Equation (34). Numerical experiments on a uniform mesh have shown that the value of β_{opt} for unsteady flow can be evaluated by the following relation:

$$\beta_{\text{opt}} = \begin{cases} \dfrac{2\Delta t}{3} & \text{if } M_0 \leq 0.05 \\ 0 & \text{otherwise} \end{cases} \tag{39}$$

where the time step is such that $\max|\Delta x_1/u_i|$ is close to 1.

By using this value of β, the efficiency of the algorithm becomes quasi independent of M_0 for unsteady flows. In fact, Figure 4 shows the CPU time required to advect the Taylor vortex on the uniform mesh described above for a reference Mach number M_0 varying from 10^{-4} to 2. The results, normalized by the CPU time required by the computation at $M_0 = 1$, demonstrate the success of the method. Note that the variations of the CPU time as a function of M_0 are in between 1 and 1.7. For the incompressible regime ($M_0 \in [10^{-4}, 0.05]$), the reference Mach number has no influence on the efficiency. In the subsonic regime ($M_0 \in [0.05, 1]$), the efficiency increase is due to the decreased problem stiffness. The efficiency decrease in the supersonic regime is caused by the neglected kinetic energy variations in the construction of the approximate Newton method. This yields an increase in the number of iterations in the Newton process.

Equation (39) is valid only if $\max(\Delta x_1/u_i)$ is near unity. When this ratio becomes larger, another rule must be found to estimate β_{opt}. Therefore, in order to evaluate the behavior of the algorithm, the Taylor vortex has been advected on a stretched mesh in the x_3-direction with a refinement near $x_3 = 0.5$ ($\Delta x_{3\ \text{min/max}} = 0.0005, 0.01$). Three different time steps, $\Delta t = 0.0005,\ 0.005,\ 0.05$, and two reference Mach numbers, $M_0 = 10^{-3}$, 0.8, have been considered.

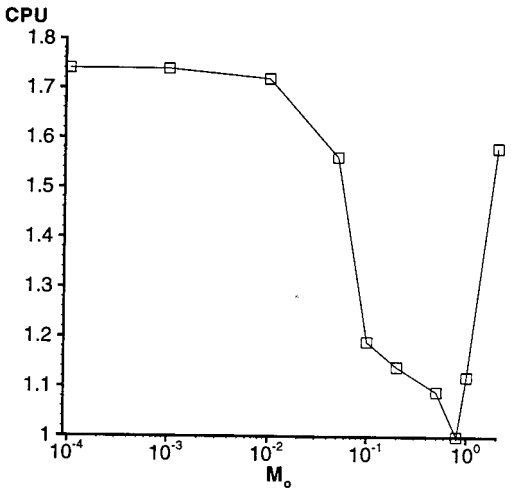

Figure 4. Taylor vortex advection: influence of the flow regime on the present method efficiency (normalized CPU time versus M_0 at $\Delta t = 0.005$).

Table I. Influence of M_0 and Δt on β_{opt} for a stretched mesh.

Δt	M_0	β_{opt}
0.0005	0.001	0.002
0.005	0.001	0.04
0.05	0.001	1.30
0.0005	0.8	0.0001
0.005	0.8	0.25
0.05	0.8	7.00

The values of β_{opt} are summarized in Table I. Even though the values of β_{opt} are greater in the compressible regime than in the incompressible one for large Δt, the results are quite surprising. Indeed, the optimal value of β is close to 7 if $\Delta t = 0.05$ and $M_0 = 0.8$, whereas this value is six times smaller for $M_0 = 0.001$. Yet, when the compressibility effect becomes important, the artificial compressibility effect must be decreased as the dynamic pressure plays an important role in the enforcement of the continuity equation. As a consequence, the value of β is not the best parameter to estimate Newton approximation due to the matrix Γ. In order to achieve a better understanding of the relationship between β_{opt}, the time step, and the mesh size on a stretched mesh, Equation (36) is rewritten as

$$(D_M^{-1} M + \epsilon_{\text{stab}} \Gamma) \Delta Q = -D_L^{-1} f_d(Q_c^l, Q_c^n, Q_c^{n-1}) \tag{40}$$

with D_M^{-1} the inverse of the main diagonal of M. The numerical parameter ϵ_{stab} is determined by the relation

$$\beta = \epsilon_{\text{stab}} \frac{\gamma M_0^2 + 2\Delta t/3 M_{\text{Euler } i,k}(1,1)}{T} \tag{41}$$

where $M_{\text{Euler } i,k}(1,1)$ is a diagonal coefficient of the first block of M_{Euler} (Equations (31)–(33)), and represents the contribution of the spatial derivative of the pressure acting on the evolution of $\rho_{i,k}$ in the continuity equation

$$M_{\text{Euler } i,k}(1,1) = \frac{1}{\Delta x_1}\left(Dp_1 + \frac{\gamma M_0^2 u_1}{T}\right) + \frac{1}{\Delta x_3}\left(Dp_3 + \frac{\gamma M_0^2 u_3}{T}\right) \tag{42}$$

As β is considered a constant in the previous cases, an estimation of ϵ_{stab} is computed with Equation (41), by assuming that $\max_{i,k} \beta$ is equal to β_{opt} in Table I. As expected, the results summarized in Table II show that the second term of the Jacobian in the Newton approximation (Equation (40)) is smaller in the compressible regime. In Table II, one can see that the values of ϵ_{stab} are of the same order as Δt for the compressible case [33]. Therefore, Γ acts like a small perturbation. With the perturbation of the diagonal term able to reach as much as 26 per cent of the exact value, the approximation turns out to be larger in the nearly incompressible case. In fact, for low M_0 values, the dynamic pressure behaves like a Lagrangian multiplier [37,38]. This tends to drive the momentum divergence to zero because its influence on the variations of ρ is not significant.

In the following numerical test cases, Equation (41) is used to obtain an estimation of β_{opt}. For incompressible cases, ϵ_{stab} is equal to 0.1 so that, on a uniform mesh, β would approximate the definition in Equation (39). For compressible cases, β_{opt} is set to 0. Note here that when no stretched grid is used (as it is here), $\epsilon_{\text{stab}} \approx \Delta t$ leads to very small values of β. Therefore, we chose to set β to 0 in order to speed up the evaluation process.

5. NUMERICAL RESULTS: VALIDATION AND DISCUSSION

In all the following test cases, the dynamic viscosity is set to a constant in order to be consistent with the benchmark models.

Table II. Evolution of ϵ_{stab} in function of Δt and M_0 for a stretched mesh.

Δt	M_0	ϵ_{stab}
0.0005	0.001	0.06
0.005	0.001	0.07
0.05	0.001	0.26
0.0005	0.8	0.0001
0.005	0.8	0.01
0.05	0.8	0.08

5.1. Nearly incompressible regime

In this part, the accuracy of the method is investigated for very low values of M_0. The first problem considered is a steady Rayleigh–Bénard flow, which allows the verification of both the accuracy of the spatial discretization and the failure of incompressible method when large temperature variations are present. The second test problem is that of the vortex shedding phenomenon around a square cylinder. This permits the evaluation of the algorithm ability to compute unsteady low-Mach number flows.

5.1.1. Rayleigh–Bénard flow. One of the goals of this paper is to illustrate the shortcomings of the classical incompressible method in accommodating very low-Mach number flows with large temperature variation. Accordingly, we use the work of Fröhlich and Gauthier [39], who were interested in natural convection occurring in an astrophysical context. Fröhlich and Gauthier [39] have employed a numerical method using low-Mach number equations [40] and a pseudo-spectral discretization, and calculated natural convection with M_0 equal to zero and large temperature variation. Their computational domain, presented in Figure 5, is a rectangle of length L and height $H = 1$. A strong temperature gradient, defined by $(T_b - T_t) = 1$, is maintained between the top and bottom walls in order to create significant compressibility effects, even at low Mach number. The hydrostatic state computed by Equation (6) is

$$T_s(z) = 1.5 - z$$

$$\rho_s(z) = (1.5 - z)^a, \quad \text{where } a = Fr\gamma M_0^2 - 1$$

The reference temperature is defined by $T_s(0.5)$. The flow parameters of the computations are summarized in Table III. Free-slip isothermal boundary conditions are applied at the top and

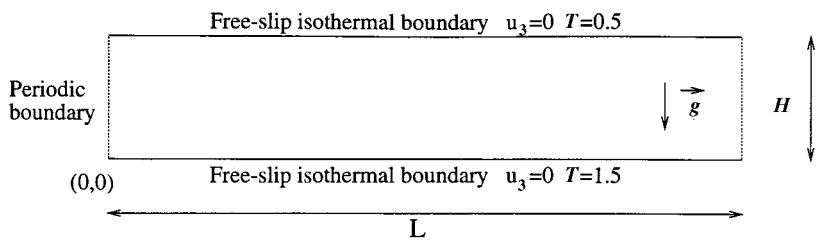

Figure 5. Problem definition.

Table III. Flow parameters.

M_0	Re	$\Delta T/T_0$	Fr	Pr	γ	L/H
0.001	87.16	1	1	0.71	1.4	2.8078

bottom surfaces, which yields $u_3 = 0$, and $\partial u_1/\partial z = 0$. Also, the temperature is fixed to its hydrostatic state value. In the x_1-direction, the flow is assumed periodic, with period length L. The initial condition used for the computation is the hydrostatic state randomly perturbed with infinitesimal amplitude (e.g., 10^{-6}). The computation is performed on a 128×101 points grid, with uniform discretization in the x_1-direction. A hyperbolic stretching is used in the x_3-direction, with refinement near the boundary. Note that the reference computation of Fröhlich and Gauthier is performed with 64×39 points, but their results are based on a Fourier–Chebyshev pseudo-spectral algorithm, characterized by a high-order accuracy. Even though this is a steady state problem, three Newton iterations are made at each time step to enhance the stability of the time integration [16,17]. The time step is set to 0.01 and approximately 14 iterations of the Bi-CGSTAB are necessary to decrease the residual by one order of magnitude. The steady state is reached after 100 time units, and the main flow is composed of a roll generated by buoyancy forces. This is illustrated in Figure 6. The accuracy of the present method can be estimated from the analysis of Table IV, where some maximum values of the flow features are compared with the results of Fröhlich and Gauthier. The Nusselt number, *Nu*, is a horizontal average of the temperature gradient at the bottom wall

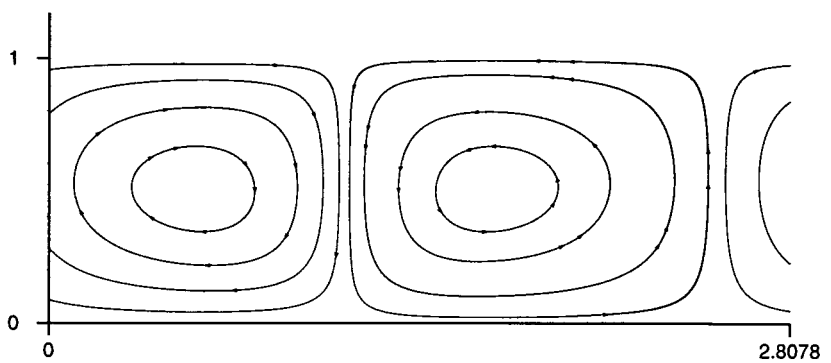

Figure 6. Streamline of the flow.

Table IV. Computed maximum flow characteristics and reference data.

References	$\lvert u\rvert_M$	$\lvert\nabla \cdot u\rvert_M$	w_M	$(p_{\mathrm{dyn}}/p_{\mathrm{s}})_M$	$((T-T_{\mathrm{s}})/T_{\mathrm{s}})_M$	$((\rho-\rho_{\mathrm{s}})/\rho_{\mathrm{s}})_M$	M_M	Nu
[39]	1.0996	1.2279	3.561	—	0.8320	0.9410	—	4.428
Present paper	1.1066 (0.6%)	1.2542 (2%)	3.590 (0.90%)	0.0007 (—)	0.8375 (0.6%)	0.9734 (3.0%)	0.0009 (—)	4.46 (0.7%)

The quantities in parentheses are the relative errors.

$$Nu = -\left\langle \frac{\partial T}{\partial z}(x, z = 0) \right\rangle_x$$

The maximum values of velocity, temperature, and Nusselt are in excellent agreement, with differences within 1 per cent. The prediction of the maximum value of the density, vorticity, and the divergence velocity is slightly less accurate with the error reaching 3 per cent. These differences could be explained by the use of a central second-order accurate spatial approximation to determine the values of the vorticity and the divergence, where another discrete approximation is used in the numerical benchmark. However, the difference in the density could also be explained by the slightly different model used in Reference [39], where the dynamic pressure is not taken into account for the determination of the density. Yet, the discrepancies in the maximum values of the flow characteristics are acceptable, especially since it is known that upwind schemes tend to undershoot or overshoot such data. Thus, we conclude that the spatial accuracy of the scheme is demonstrated in the low Mach number regime. Additionally, it is interesting to note that the maximum value of the divergence of the velocity field is close to 1.2, despite the very low value of the Mach number in the entire flow field. Therefore, this kind of flow cannot be computed by an incompressible approach. The present method, however, is able to deal with a broad range of stratified flow conditions, including strong temperature variations.

5.1.2. Vortex-shedding flow past a square cylinder. The computation of the flow past a square cylinder is chosen to demonstrate the ability of the present method to accurately simulate nearly incompressible unsteady flows. Again, experimental and numerical data in the laminar regime are available in the literature [41–43]. Experimental results, however, do not provide an appropriate database for the validation of the method. Also, Sohankar *et al*. [41] show that the vortex-shedding frequency is strongly influenced by the boundary conditions and the blockage coefficient (the ratio between the height of the cylinder and the height of the computational domain). Therefore, the computational domain and boundary conditions, employed in Reference [42], are retained (see Figure 7) for this test case in order to ensure that the comparisons of vortex-shedding frequency with the reference results [42] are not perturbed by boundary conditions and blockage coefficient. The reference length is the size of the cylinder ($D = 1$), and the reference velocity is the fluid velocity at the inlet. At $x_3 = 0$ or $x_3 = 12$, the vertical velocity, normal derivative of u_1 and T are set to zero. At the outlet, u_3, the normal derivative of u_1 and the dynamic pressure residuals are set to zero during the computation. Two values of the Reynolds number, based on the inlet velocity and D, are considered: $Re = 100$ or $Re = 300$. The Prandtl number is set to 0.71, and the reference Mach number M_0 is equal to 0.001. As the frequency is influenced by the size of the mesh near the cylinder, a stretched 220×200 points grid is used in both directions, with $\Delta x_{1\ \min} = \Delta x_{3\ \min} = 0.004$ and $\Delta x_{1\ \max} = \Delta x_{3\ \max} = 0.8$. The initial condition for the computation is a uniform field: $u_1 = 1,\ u_3 = 0,\ p_{\mathrm{dyn}} = 0,\ T = 0$. The time step is set to 0.03 (a first-order accurate temporal derivative approximation is used in Reference [42] with $\Delta t = 0.025$) and an average of six Newton iterations are made, as soon as the transient phenomena due to the initial condition are eliminated. Two snapshots of the vorticity field illustrating the main features of the flow are shown in Figure 8 for $t = 100$ and 300 and for the lower Reynolds case. In a first phase, a nearly stationary solution of the flow is obtained around $t = 100$. However, this symmetric solution is lost because of numerical error

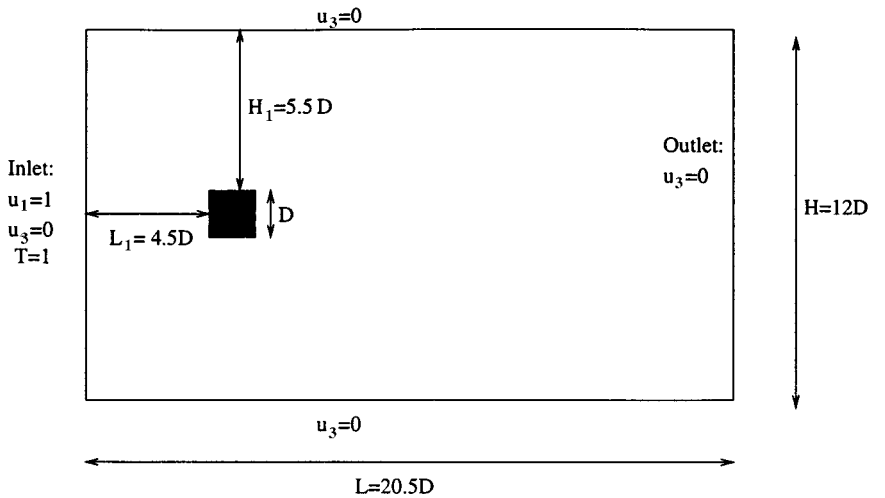

Figure 7. Problem definition.

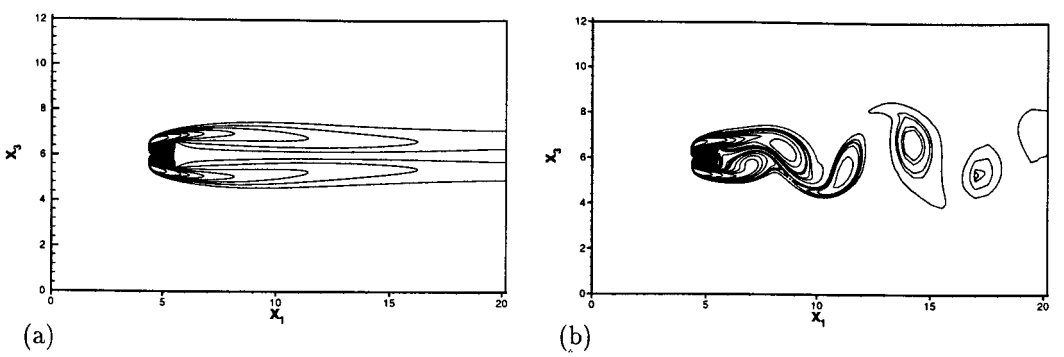

Figure 8. $Re = 100$, vorticity contours: (a) $t = 100$, (b) $t = 300$.

accumulation and consequently vortex-shedding appears after $t = 120$. The observation of Figure 9, showing the time history of the lift and drag owing to pressure, allows differentiation between these different phases. The influence of the viscous effects on the drag and lift coefficient are within 2 per cent [42] of the global values. At the beginning of the computation, the lift coefficient is zero, showing the symmetry of the solution, whereas strong variations of the drag coefficient are present due to the large value of the initial velocity divergence field. After a transitional period, between $t = 120$ and 200, a periodic solution is obtained. A Fourier analysis of the lift coefficient, between $t = 220$ and 320, gives a Strouhal number of 0.156, compared with 0.154 obtained in the reference data [42]. The average value of the drag (equal

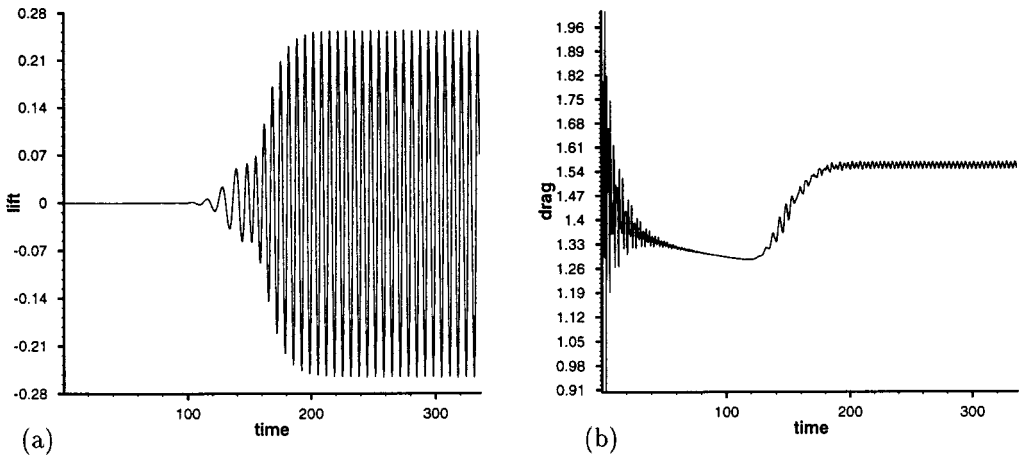

Figure 9. $Re = 100$: (a) lift history, (b) drag history.

to 1.55) and the amplitude of the lift coefficient (close to 0.24) agree well with the reference data. For the $Re = 300$ case, the flow possesses the same properties, but the lift amplitude and average value of the drag are increased. Figure 10 shows the behavior of the lift coefficient. The Fourier analysis is performed between $t = 450$ and 600 to eliminate the presence of spurious frequencies due to the transitional phase in the lift spectrum. The temporal average of drag coefficient, between $t = 450$ and 600, is equal to 1.92, compared with 1.89 obtained in

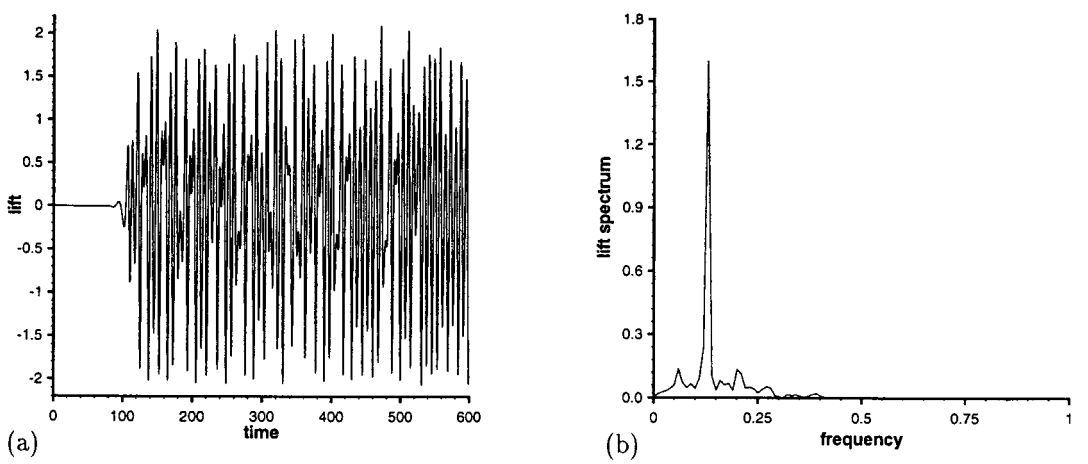

Figure 10. $Re = 300$: (a) lift history, (b) drag history.

the reference data. Moreover, as mentioned in Reference [42], the signal is not fully periodic, but a dominant frequency equals to 0.129 can be easily extracted from the lift spectrum. A Strouhal number of 0.130 is found, which is in very good agreement with the reference data. In Reference [44], it is shown that the lost of the signal periodicity is due to the bi-dimensional character of the computations. Therefore, the prediction of vortex-shedding frequency for different values of the Reynolds number demonstrates the ability of the present method to simulate unsteady low-Mach number flows.

5.2. Compressible regime

The AUSM+ scheme has shown its accuracy for the computation of subsonic or supersonic flow [25,26]. The aim of this section is to show that the modifications, introduced to alleviate accuracy problems in the incompressible regime, do not degrade the performance of the original scheme for compressible flows. As these modifications do not change the scheme in the supersonic regime, only subsonic and transsonic flows are computed.

5.2.1. Subsonic compressible mixing layer. Computations of compressible mixing layer are carried out to evaluate the temporal and spatial accuracy of the present method in the absence of shocks. The initial growth of the mixing layer provides information on the spatial and temporal accuracy of the method, where the accuracy of different limiters is assessed in a transsonic regime (see Reference [45]). A reference solution is produced by using a sixth-order accurate Hermitian scheme [46] for the spatial derivative, with a third-order accurate compact Runge–Kutta scheme for the temporal integration [47]. The mean profiles of velocity and temperature are specified by the following relations:

$$u_1(x_1, x_3, t = 0) = 0.5 \tanh(2(x_3 - 13))$$

$$T(x_1, x_3, t = 0) = 1 + M_0^2 \frac{\gamma - 1}{2} (1 - u_1)^2$$

where x_1 and x_3 are varying from 0 to 20 and 26 respectively. The Prandlt number is assumed to be unity and the pressure is assumed to be uniform at the initial time. The reference temperature and velocity are based on the upper free stream temperature and the initial vorticity thickness respectively. The Mach number M_0 is 0.8 and the Reynolds number is 400. The flow is periodic in the streamwise x_1-direction and free-slip boundary conditions are imposed in the normal direction, x_3. The vorticity thickness of the mixing layer is defined as

$$\delta_w = \left(\mathrm{Max}_{x_3} \left| \frac{\partial \langle u_3 \rangle_{x_1}}{\partial x_3} \right| \right)^{-1}$$

with $\langle u_3 \rangle_{x_1}$ being the spatial average in the homogeneous direction x_1. A uniform discretization is adopted in both directions. The reference solution is obtained on a 300×300 regular Cartesian mesh grid, whereas the accuracy of the present scheme is assessed on a 150×150 and 75×75 grids. Since the flow is linearly unstable, the instability is forced by adding small perturbations, u_1' and u_3', to the initial mean velocity

$$u_1'(x_1, x_3) = 0.05 \frac{x_3 - 13}{2\pi} \sin\left(\frac{\pi x_1}{10}\right) \exp\left(-\frac{(x_3 - 13)^2}{10}\right)$$

$$u_3'(x_1, x_3) = 0.05 \cos\left(\frac{\pi x_1}{10}\right) \exp\left(-\frac{(x_3 - 13)^2}{10}\right)$$

A time step $\Delta t = 0.03$ is used for the reference computation in order to satisfy the CFL condition. Different time steps are employed in the implicit integration $\Delta t = 0.03,\ 0.06$ and 0.1. For this case, the solution after the first time step is obtained by the explicit temporal integration. Indeed, Equation (20) requires two initial conditions. At $t^n = 0$, one can assume that the same initial condition can be imposed at t^n and t^{n-1}. However, this is equivalent to forcing the instability with different u_1' and u_3' than the reference computation. Then, the growth of the vorticity thickness is perturbed, and comparisons between the reference results and those obtained with the present method are not valid. Thus, the solution at $t = \Delta t$ is achieved by the Runge–Kutta scheme, when the present method is employed for the temporal integration. The time integration is set to 100, and approximately four Newton iterations are required at each time step, one or two iterations of Bi-CGSTAB are required. A visualization of the vorticity is shown in Figure 11(a) at the end of the computation. The growth of the vorticity thickness is plotted in Figure 11(b) for computations carried out on the 150×150 grid using different values of the time step. It appears that the non-linear phase starts quickly ($t = 20$), and the large value of the perturbations u_1' and u_3' can explain why the period of linear growth of the vorticity thickness is so short. Since the solution is almost independent of the time step and discrepancies with the reference computation are not significant, the

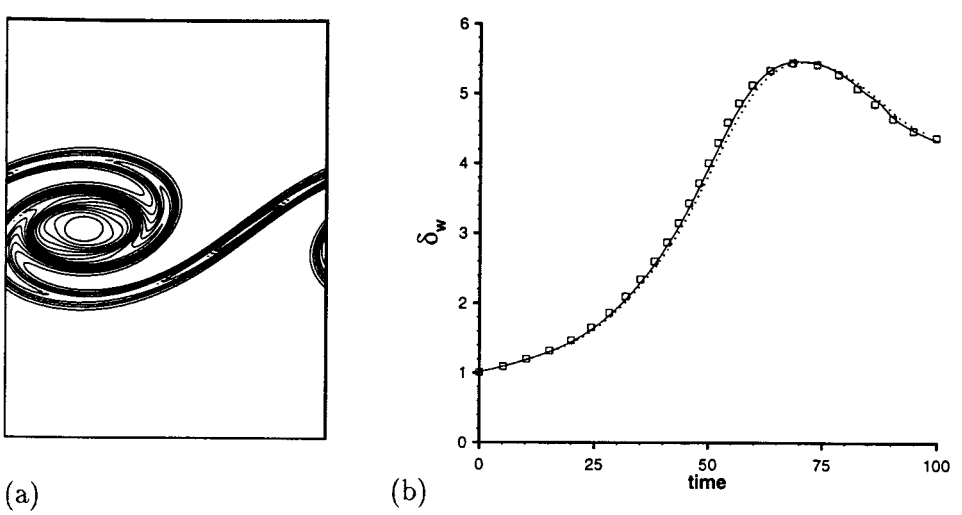

Figure 11. (a) Snapshot of vorticity at $t = 100$. (b) Time history of vorticity thickness (δ_w versus time). Reference solution: □; present method (150×150 grid): · · · , $\Delta t = 0.06$; - - - , $\Delta t = 0.4$; —, $\Delta t = 0.03$.

temporal accuracy of the present method is clearly demonstrated for this case. In fact, small differences appear between the computations with $\Delta t = 0.06$ or 0.1, but the solutions obtained with $\Delta t = 0.03$ and 0.06 cannot be distinguished. The spatial accuracy can be studied by looking at Figure 12, where vorticity distribution at $x_3 = 13$ and the influence of mesh refinement on the time evolution of the vorticity thickness are shown. On the coarse grid, the effect of numerical dissipation becomes noticeable, where all extrema of the vorticity distribution are significantly underpredicted, but the growth of the vorticity thickness is slowed down [45]. However, results on the 150×150 grid are in very good agreement with the reference computation, showing the accuracy of the present method in the case of subsonic flow.

5.2.2. Shock/spot interaction. The aim of this numerical test case is to demonstrate that the modifications introduced in the AUSM+ scheme still allow the computation of unsteady flows, including shocks. The advection of a Gaussian temperature spot through a straight shock is considered. Numerical results are given by Garnier *et al.* [48], who assessed the accuracy of high-order shock-capturing schemes. The results of the present method are compared with those obtained by the fourth-order accurate weighted essentially non-oscillatory (WENO) scheme [49], and the Runge–Kutta scheme mentioned in the previous section. The computational domain is a rectangle of height $H = 1$ and length $L = 2H$. A shock of strength $p_{\text{front}}/p_{\text{back}} = 0.4$, which implies $M_0 = 1.1588$, is initialized at $x_1 = 1$. The Reynolds number is based on the inlet velocity and $H = 2000$, and the Prandlt number is set to 0.7. A Gaussian temperature spot, T_{spot}, is added to the temperature field, in front of the shock. This spot, located at $(x_1, x_3) = (0.5, 0.5)$, is specified by the following relation:

$$T_{\text{spot}}(x_1, x_3) = a_1^{-4}(r^2 - a_1^2)^2 \exp(-r^2/a_2)$$

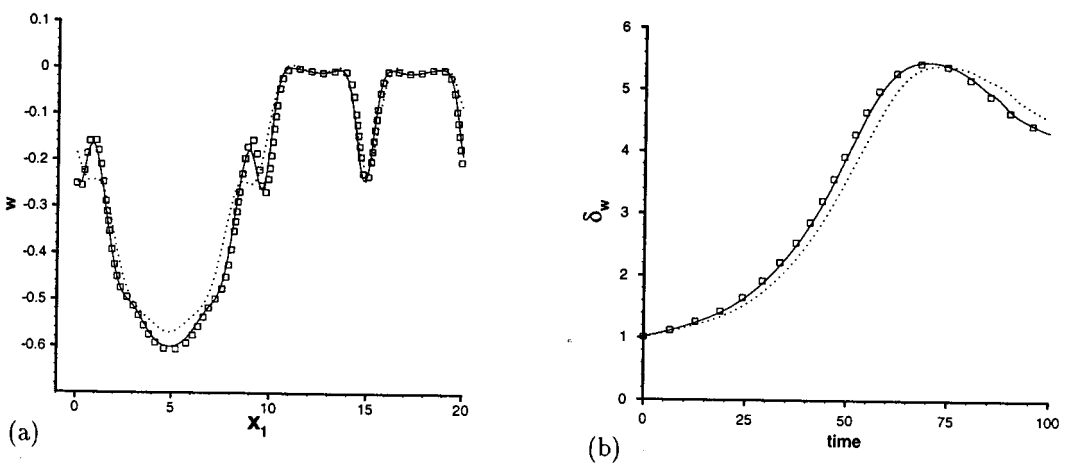

Figure 12. Reference solution: □; present method: —, 150×150 grid; · · ·, 75×75 grid. (a) Vorticity distribution versus x_1 co-ordinate for $x_3 = 13$. (b) Time history of vorticity thickness (δ_w versus time).

$$r = ((x_1 - 1/2)^2 + (x_3 - 1/2)^2)^{1/2}, \quad a_1 = 7, \quad a_2 = 0.07$$

The spot is advected in the streamwise direction, x_1, and the flow is periodic in the normal direction, x_3. At the outlet, zero normal derivative of each variable is imposed. A Dirichlet condition is employed at the inlet. As in Reference [48], the computations are made on a 200×100 regular grid. The time step is set to 0.005 and the period of the computation is set to unity. Three Newton iterations are performed at each time step, whereas one or two Bi-CGSTAB iterations are required to solve the linear system. A Minmod limiter [31] is employed in the present calculations to prevent numerical oscillations near the shock. This limiter introduces a numerical parameter Θ, the compression factor, varying from 1 to 4, which renders the numerical dissipation of the limiter larger for decreasing values of Θ. In Figure 13, two snapshots of the streamwise distribution of the density at $x_3 = 0.5$ are shown for the initial and final time, illustrating the location of the temperature spot. The crossing of the shock by the temperature spot at time 0.5 leads to its deformation, which is characterized by the increase of the baroclinic torque $-(1/\rho^2)\nabla p \times \nabla \rho$ and the formation of two counter-rotative vortices behind the shock. This is illustrated by the time history of the baroclinic torque and the L_2-norm of the vorticity field plotted in Figure 14. Since the reference results are recovered near the shock, and regardless of the value of Θ (see Figure 13(b)), we estimate that the ability of the present method to deal with shocks has been demonstrated. Yet, the accuracy of the computation depends on the compression factor. For example, the extrema of density distribution and baroclinic torque are underpredicted by 10 per cent for $\Theta = 1$, whereas greater values of Θ lead to a good prediction of these extrema. However, the time history of both $|w|_2$ and the baroclinic torque are inaccurate for the larger value of Θ after $t = 0.5$. Indeed, the vorticity still increases and the value of baroclinic torque does not go to zero at the

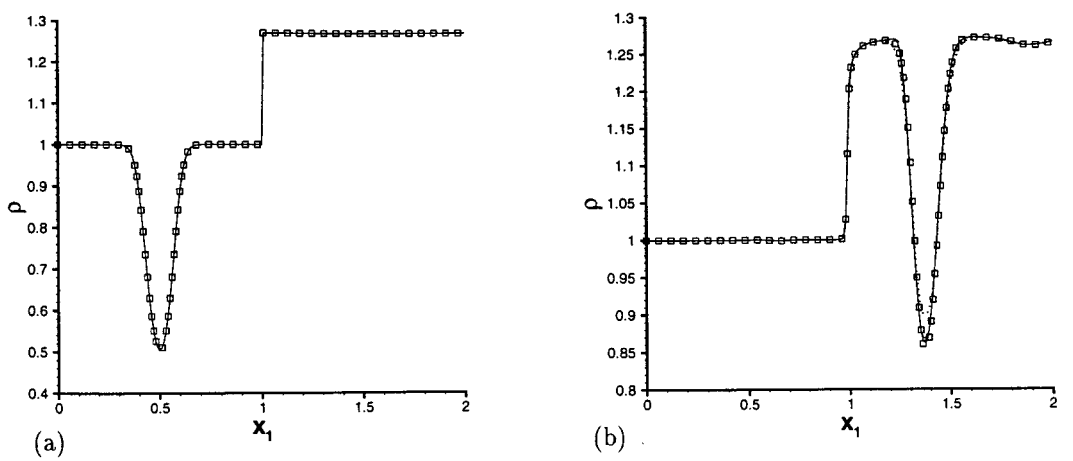

Figure 13. Density distribution at $x_3 = 0.5$ (ρ versus x_1). Reference solution, □; present method: —, $\Theta = 4$; - - - , $\Theta = 2$; · · · , $\Theta = 1$. (a) Initial time, (b) final time.

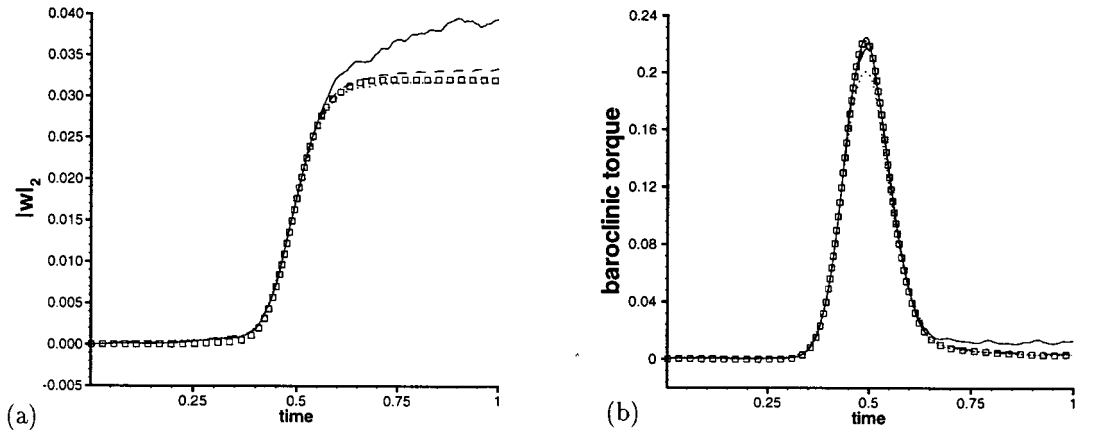

Figure 14. Reference solution, □; present method: —, $\Theta = 4$; - - - , $\Theta = 2$; · · · , $\Theta = 1$. (a) Time history of vorticity L_2-norm; (b) Time history of baroclinic torque.

end of the computation. This inaccurate behavior of the least dissipative scheme is due to the presence of oscillations near the shock for some values of x_3. This prevents the cancellation of the baroclinic term. Finally, the choice $\Theta = 2$, which allows a good compromise between the resolution of the shock and the error on the calculation of the extrema, demonstrates the ability of the present method to compute unsteady transsonic flow including shocks. The results could be improved by the use of a more accurate limiter.

6. CONCLUDING REMARKS

A second-order accurate implicit method has been developed for solving unsteady, compressible, viscous, stratified flows at all speeds. The temporal integration is achieved by an approximate Newton method, based on artificial compressibility. This technique overcomes the numerical stiffness of the compressible Navier–Stokes equations at low Mach number. Additionally, a modified AUSM+ scheme is employed for the Euler fluxes in order to allow computations of flows including shocks, and still maintains the spatial accuracy of the method in the nearly incompressible regime. This approach achieves a good compromise between robustness, efficiency, and accuracy for the whole range of Mach numbers. In addition, no approximation is required to model stratification effects rendering the method more accurate and general than those based on asymptotic development or Boussinesq linearization. As the solution of the linear system is crucial for the efficiency of the method, future work includes improving the Jacobi preconditioning [26] in order to allow the extension of the current model to three-dimensional computations on stretched grids.

REFERENCES

1. Choi YH, Merkle CL. The application of preconditioning in viscous flow. *Journal of Computational Physics* 1993; **105**: 207–223.
2. Turkel E. Preconditioned methods for solving the incompressible and low speed compressible equations. *Journal of Computational Physics* 1987; **72**: 277–298.
3. Erikson LE. A preconditioned Navier–Stokes solver for low Mach number flows. In *Proceedings of Computational Fluid Dynamics '96*, Désidéri JA, Pandolfi M, Périaux J (eds). Wiley: Chichester, 1996; 199–205.
4. Lee D. Local criteria for local Euler preconditioning. *Journal of Computational Physics* 1998; **144**: 423–459.
5. Strang G. On the construction and comparisons of difference schemes. *SIAM Journal of Numerical Analysis* 1968; **5**: 506–517.
6. Erlebacher G, Hussaini MY, Kreiss HO, Sarkar S. The analysis and simulation of compressible turbulence. ICASE Report 90-15, Hampton, VA, 1990.
7. Codina R, Vasquez M, Zienkiewicz OC. General algorithm for compressible and incompressible flows. Part III: the semi-implicit form. *International Journal of Numerical Methods in Fluids* 1998; **27**: 13–32.
8. Karki KC, Patankar SV. Pressure based calculation procedure for viscous flows at all speeds in arbitrary configurations. *AIAA Journal* 1989; **27**: 1167–1174.
9. Demirdzic I, Lilek Z, Peric M. A collocated finite volume method for predicting flows at all speeds. *International Journal of Numerical Methods in Fluids* 1993; **16**: 1029–1050.
10. Bijl H, Wesseling P. A unified method for computing incompressible and compressible flows in boundary-fitted coordinates. *Journal of Computational Physics* 1998; **141**: 153–173.
11. Shuen JS, Chen KH, Choi Y. A coupled implicit method for chemical non-equilibrium flows at all speeds. *Journal of Computational Physics* 1993; **106**: 306–318.
12. Pletcher RH, Chen KH. On solving the compressible Navier–Stokes equation for unsteady flows at very low Mach numbers. AIAA Paper No. 93-3368, 1993.
13. Wang WP. Coupled compressible and incompressible finite volume formulations for LES of turbulent flow with and without heat transfer. PhD thesis, Iowa State University, Ames, IA, 1995.
14. Venkateswaran S, Merkle CL. Dual time stepping and preconditioning for unsteady computations. AIAA Paper No. 95-0078, 1995.
15. Dailey LD, Pletcher RH. Evaluation of multigrid acceleration for preconditioned time-accurate Navier–Stokes algorithms. *Computers and Fluids* 1996; **25**: 791–811.
16. Buelow PEO, Schwer DA, Feng J, Merkle CL. A preconditioned dual-time, diagonalized ADI scheme for unsteady computations. AIAA Paper No. 97-2101, 1997.
17. Mary I, Sagaut P, Deville M. An algorithm for low Mach number unsteady flows. *Computers and Fluids* 2000; **29**: 119–147.
18. Turkel E, Fiterman A, van Leer B. Preconditioning and the limit to the incompressible flow equations. ICASE Report No. 93-42, 1993.
19. Edwards JR, Liou MS. Low-diffusion flux-splitting methods for flows at all speeds. *AIAA Journal* 1998; **36**: 1610–1617.
20. Guillard H, Viozat C. On the behaviour of upwind schemes in the low Mach number limit. *Computers and Fluids* 1999; **28**: 63–86.
21. Turkel E, Radespiel R, Kroll N. Assessment of preconditioning methods for multidimensional aerodynamics. *Computers and Fluids* 1997; **26**: 613–634.
22. van der Vorst H. Bi-CGSTAB: a fast and smoothly converging variant of Bi-CG for the solution of nonsymmetric linear systems. *SIAM Journal of Scientific and Statistical Computing* 1992; **13**: 631–644.
23. Chorin AJ. A numerical method for solving incompressible viscous flow problems. *Journal of Computational Physics* 1967; **2**: 12–26.
24. Mary I, Sagaut P, Deville M. An assessment of some algorithm for steady and unsteady low Mach number flows. In *Proceedings of ICFD 6th International Conference on Numerical Methods for Fluid Dynamics*, Baines MJ (ed.). Will Print: Oxford, 1998; 403–409.
25. Liou MS. A sequel to AUSM: AUSM+. *Journal of Computational Physics* 1996; **129**: 364–382.
26. Luo H, Baum JD, Löhner R. A fast matrix-free implicit method for compressible flows on unstructured grids. *Journal of Computational Physics* 1998; **146**: 664–690.
27. Sesterhenn J, Muller B, Thomann H. On the cancellation problem in calculating compressible low Mach number flows. *Journal of Computational Physics* 1999; **151**: 597–615.
28. Spiegel EA. Convective instability in a compressible atmosphere. *Astrophysics Journal* 1965; **141**: 1068–1090.
29. Volpe G. On the use and accuracy of compressible flow codes at low Mach numbers. AIAA Paper No. 91-1662, 1991.

30. Wang ZJ. A fast flux-splitting for all speed flow. In *Proceedings of 15th International Conference on Numerical Methods in Fluid Dynamics*, Monterey, CA, Kutler P (ed.). Springer: New York, 1996; 141–146.
31. Yee HC. Construction of explicit and implicit symmetric TVD schemes and their applications. *Journal of Computational Physics* 1987; **68**: 664–690.
32. Melson ND, Sanetrik MD, Atkins HL. Time-accurate Navier–Stokes calculations with multigrid acceleration. In *Proceedings of the 6th Copper Mountain Conference on Multigrid Methods*, Melson ND, Copper Mountain, CO (ed.), 1993; 423–437.
33. Pulliam TH. Time accuracy and the use of implicit methods. AIAA Paper No. 93-3360, 1993.
34. Lascaux P, Théodore R. *Analyse numérique matricielle appliquée à l'art de l'ingénieur (tome 2)*. Masson: Paris, 1987.
35. Liou MS, van Leer B. Choice of implicit and explicit operator for the upwinding differencing method. AIAA Paper No. 88-0624, 1988.
36. Orkwis PD. Comparison of Newton's and quasi-Newton's method solvers for the Navier–Stokes equations. *AIAA Journal* 1993; **31**: 832–836.
37. Peyret R, Taylor TD. *Computational Methods for Fluid Flow*. Springer: New York, 1983.
38. Merkle CL, Athavale M. Time-accurate unsteady incompressible flow algorithms based on artificial compressibility. AIAA Paper No. 87-1137, 1987.
39. Fröhlich J, Gauthier S. Numerical investigations from compressible to isobaric Rayleigh–Bénard convection in two dimensions. *European Journal of Mechanics*, *B Fluids* 1993; **12**: 141–159.
40. Rehm RG, Baum HR. The equations of motion for thermally driven buoyant flows. *Journal of Research of the National Bureau of Standards* 1978; **83**: 297–308.
41. Sohankar A, Norberg C, Davidson L. Low-Reynolds-number flow around a square cylinder at incidence: study of blockage, onset of vortex-shedding and outlet boundary condition. *International Journal of Numerical Methods in Fluids* 1998; **26**: 39–56.
42. Franke R, Rodi W, Schönung B. Numerical calculation of laminar vortex-shedding flow past cylinders. *Journal of Wind Engineering and Industrial Aerodynamics* 1990; **35**: 237–257.
43. Davis RW, Moore EF. A numerical study of vortex-shedding from rectangles. *Journal of Fluid Mechanics* 1982; **116**: 475–506.
44. Sohankar A, Norberg C, Davidson L. Simulation of three-dimensional flow around a square cylinder at moderate Reynolds numbers. *Physics and Fluids* 1999; **11**: 288–306.
45. Sandham ND, Yee HC. A numerical study of a class of TVD schemes for compressible mixing layers. NASA TM-102194, 1989.
46. Lele SK. Compact finite difference schemes with spectral-like resolution. *Journal of Computational Physics* 1992; **103**: 16–42.
47. Shu S, Osher S. Efficient implementation of essentially non-oscillatory shock-capturing schemes, II. *Journal of Computational Physics* 1988; **77**: 439–471.
48. Garnier E, Sagaut P, Comte P. ENO and PPM schemes for direct numerical simulation of compressible flows. In *Advances in DNS/LES*, Liu C, Liu Z (eds). Greyden Press: Ruston, USA, 1997; 589–596.
49. Liu XD, Osher S, Chan T. Weighted essentially non-oscillatory shock-capturing schemes. *Journal of Computational Physics* 1994; **115**: 200–212.

